

## Quantum process tomography of a Mølmer-Sørensen interaction

Nir Navon,<sup>\*†</sup> Nitzan Akerman,<sup>\*</sup> Shlomi Kotler,<sup>‡</sup> Yinnon Glickman, and Roee Ozeri

Department of Physics of Complex Systems, Weizmann Institute of Science, Rehovot 76100, Israel

(Received 20 September 2013; revised manuscript received 24 March 2014; published 28 July 2014)

We present a simple tomographic protocol, for two-qubit systems, that relies on a single discriminatory transition and no direct spatially selective imaging. This scheme exploits excess micromotion in the trap to realize all operations required to prepare all input states and analyze all output states. We demonstrate a two-qubit entangling gate with a Bell state production fidelity of 0.981(6), and apply the above protocol to perform the first quantum process tomography of a Mølmer-Sørensen entangling gate. We characterize its  $\chi$ -process matrix, the simplest for an entanglement gate on a separable-states basis, and observe that our dominant source of error is accurately modeled by a quantum depolarization channel.

DOI: [10.1103/PhysRevA.90.010103](https://doi.org/10.1103/PhysRevA.90.010103)

PACS number(s): 03.65.Wj, 03.67.Mn, 37.10.De, 42.50.Ct

The ability to realize and characterize high-fidelity two-qubit entangling gates is central for quantum information science as, together with single-qubit rotations, they can form a so-called universal quantum gate set for quantum computation [1]. The detailed characterization of these gates is therefore crucial. Quantum process tomography (QPT) is a systematic method allowing one to fully characterize linear quantum processes. In particular, QPT of two-qubit entangling gates has been used to characterize controlled-NOT (CNOT) gates in linear-optic [2], NMR [3], as well as trapped-ion qubits [4,5], or a square root  $i$ -SWAP gate with superconducting qubits [6]. In trapped-ion experiments, Mølmer-Sørensen (MS) entangling gates [7] have become increasingly popular, both for quantum computation purposes [8–10] and for inducing effective spin-spin couplings that allow one to simulate complex quantum many-body Hamiltonians from condensed matter physics [11]. One of its main advantages as compared with other gate protocols is its first-order insensitivity to the phonon occupation number (i.e., temperature of the ion crystal), which allowed, *inter alia*, the highest entangled state production fidelity reached to date [0.993(1) [12]], entanglement between ions in thermal motion [13], as well as the creation of a maximally entangled state of a large ( $N = 14$ ) number of qubits [14]. In this Rapid Communication, we first implement a new and simple protocol for QPT with trapped ions, which only requires a single discriminatory transition. The scheme is based on inhomogeneous micromotion in the trap that enables addressing single qubits in the chain [15–17]. Subsequently, we realize the first full tomographic reconstruction of a Mølmer-Sørensen interaction which, despite its growing importance, has not been process-analyzed yet.

A quantum process is defined as a completely positive map  $\mathcal{E}$  in the space of density matrices. Given a complete set of operators  $\{A_i\}$  (such that  $\sum_j A_j^\dagger A_j = I$ ), the output state for an arbitrary input state  $\rho$  can be written as (for details see, for

instance [3,18,19])

$$\mathcal{E}[\rho] = \sum_{a,b} \chi_{ab} A_a \rho A_b^\dagger. \quad (1)$$

Here  $\{\chi_{ab}\}$  is the *process matrix* (with  $4^n \times 4^n$  elements for  $n$  qubits), which contains the full information on the process  $\mathcal{E}$  and is measured by QPT. A convenient set of input states for tomography is the set of product states  $|\psi_i\rangle = |\phi_1\rangle \otimes |\phi_2\rangle$ , where  $|\phi_1\rangle, |\phi_2\rangle \in \{|x\rangle, |y\rangle, |z\rangle, |\bar{z}\rangle\}$ , which are the one-qubit eigenstates of the Pauli matrices  $\{\sigma_x, \sigma_y, \sigma_z, \sigma_z\}$  with eigenvalues  $\{1, 1, 1, -1\}$ . Note that, with this choice, entangled states are not used as input states. The measurement basis is conveniently chosen to be  $\sigma_i \otimes \sigma_j$  where  $i \in \{0, x, y, z\}$ , and  $\sigma_0 = I$ . However, in the experiment, the detection scheme relies on the statistics of fluorescence photons, which corresponds to the measurement of the expectation value  $\langle \sigma_z \otimes \sigma_z \rangle = \text{Tr}[\rho(\sigma_z \otimes \sigma_z)]$ . In order to measure the expectation value of  $\langle \sigma_i \otimes \sigma_j \rangle$ , we perform additional rotations on the two qubits. In general these rotations require single-qubit addressing capability. For our purpose, a single discriminatory transition is sufficient for all the required operations.

In our setup, we use  $^{88}\text{Sr}^+$  ions confined in a linear Paul trap [20]. We work with optical qubits that are encoded in the  $|S\rangle = 5S_{1/2, +1/2}$  ground-state level and in the  $|D\rangle = 4D_{5/2, +3/2}$  metastable level which has a  $1/e$  lifetime of 390 ms [21] [see Fig. 1(a)]. Coherent manipulation of the qubit state is performed with a narrow linewidth laser at 674 nm (fast linewidth of  $\sim 80$  Hz [22]) which drives an electric-quadrupole transition. The other Zeeman level of the ground state  $|S'\rangle = 5S_{1/2, -1/2}$ , separated by 12.3 MHz from the  $|S\rangle$  level due to a constant magnetic field ( $B_0 \approx 0.44$  mT), is used as an auxiliary level in the state detection scheme. Measuring the qubit state is accomplished by counting fluorescence photons on the  $5S_{1/2} \rightarrow 5P_{1/2}$  dipole transition with a photomultiplier tube. We inferred the number of ions in the  $|S\rangle$  (bright) state, for each realization, by the number of detected photons. The probabilities  $P_0$ ,  $P_1$ , and  $P_2$ , of finding zero, one, and two ions in the  $|S\rangle$  (bright) state were estimated by the fraction of realizations with the corresponding number of ions inferred in that state. The discriminatory transition is provided through a micromotion sideband. If the two-ion chain is axially aligned so that one ion sits on the rf null, the other ion is the only one to possess micromotion sidebands, on

<sup>\*</sup>These authors contributed equally to this work.

<sup>†</sup>Present address: Cavendish Laboratory, University of Cambridge, J.J. Thomson Ave., Cambridge CB3 0HE, United Kingdom; nn270@cam.ac.uk

<sup>‡</sup>Present address: Physical Measurement Laboratory, National Institute of Standards and Technology, Boulder, Colorado 80305, USA.

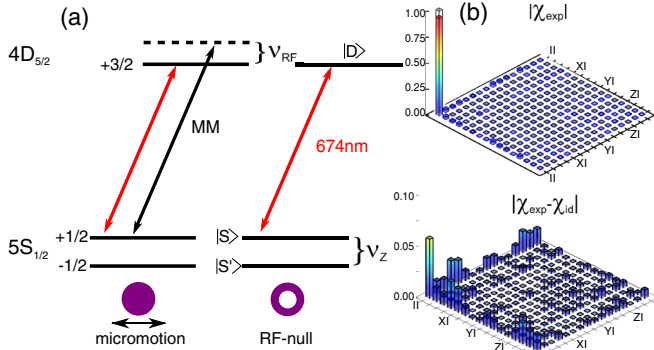


FIG. 1. (Color online) Two-qubit quantum process tomography. (a) Energy level diagram of the two ions, with the micromotion (MM) sideband (shown as a dashed black line) for the ion not sitting on the rf null, separated by  $\nu_{\text{rf}} = 21.75$  MHz from the carrier transition. The ground-state levels  $|S\rangle$  and  $|S'\rangle$  are Zeeman split by  $\nu_Z = 12.3$  MHz. (b) Absolute value of the reconstructed  $\chi$  matrix of the identity process  $|\chi_{\text{exp}}|$  and the absolute value of the difference with the ideal identity process  $|\chi_{\text{exp}} - \chi_{\text{id}}|$ . The basis of the matrix is  $\sigma_i \otimes \sigma_j$  where, for clarity we use the convention  $X = \sigma_x$ ,  $Y = \sigma_y$ ,  $Z = \sigma_z$ .

which selective quantum control can be performed [17,23], and we use here the micromotion sideband associated with the motional carrier transition [dashed energy level in Fig. 1(a)]. To maintain coherence throughout the experimental sequence, the trap rf and the signals feeding the acousto-optic modulator (AOM) that drive both the micromotion sideband and the carrier transition, are all phase-locked to a common time base provided by a commercial Rb atomic reference.

In order to measure all necessary expectation values, it is enough to possess single-qubit rotation capability on one qubit only. We look for an operation  $R_{ij}$  such that  $R_{ij}^\dagger(\sigma_i \otimes \sigma_j)R_{ij} = \sigma_z \otimes \sigma_z$ . Indeed,  $R_{ij}$  can be decomposed in the form  $R_{ij} = G_{\alpha(i,j)}L_{\beta(i,j)}$ , where  $G(L)$  is a global (local) rotation around a direction lying in the  $(x,y)$  plane of the optical qubit Bloch sphere. More precisely, these operators can be written as  $G_\alpha = \exp(i\frac{\pi}{4}\sigma_\alpha^{(1)}) \otimes \exp(i\frac{\pi}{4}\sigma_\alpha^{(2)})$ , a global  $\pi/2$  rotation around the  $\alpha$  axis, and  $L_\beta = I^{(1)} \otimes \exp(i\frac{\pi}{4}\sigma_\beta^{(2)})$ , a local  $\pi/2$  rotation around the  $\beta$  axis of only one ion, where  $\alpha, \beta = \pm x, \pm y$ . For example  $R_{xy} = G_{-y}L_x$ ,  $R_{zx} = L_{-y}$ ,  $R_{xz} = G_{-y}L_y$ , and so on. Similarly, the state preparation of all product states mentioned above can be realized using the same set of operations after initializing the ions to  $|z\rangle \otimes |z\rangle$  by optical pumping. Lastly, the value of  $\langle \sigma_z \otimes \sigma_z \rangle = P_0 + P_2 - P_1$  is extracted from fluorescence histograms. In addition, some of the necessary measurements for QPT are of the form  $I \otimes \sigma_j$  or  $\sigma_j \otimes I$ , and thus require one to measure separately the state of each ion. To perform these measurements we utilize the auxiliary  $|S'\rangle$  level to which we transfer one of the ions into a definitely bright state ( $|S\rangle$ ,  $|S'\rangle$ ). This is accomplished by first transferring the  $|S\rangle$  state population into  $|S'\rangle$  for both ions with an rf  $\pi$  pulse. Then another  $\pi$  pulse on the micromotion sideband transfers the  $|D\rangle$  state population of that ion into  $|S\rangle$ . The state of the ion at the null is then determined by  $P_2$  ( $P_0 = 0$ ). Similarly, the state of the ion with micromotion sideband is determined by applying an additional global carrier pulse to both ions.

Using all the above, we first validate our QPT toolbox by characterizing the identity process. We reconstruct the  $\chi$  matrix from the state tomography of the 16 output density matrices [19], and use a maximum likelihood process estimation [24] in order to obtain a physical matrix (noise and systematic errors lead to unphysical algebraically calculated  $\chi$  matrices, i.e., not completely positive maps). Figure 1(b) shows both the absolute value of the resulting process matrix  $|\chi_{\text{exp}}|$  and the absolute value of difference between the experimentally obtained matrix and the ideal matrix  $|\chi_{\text{exp}} - \chi_{\text{id}}|$ . Here, the values of the imaginary part are small ( $< 0.02$ ). The definition of proper (and simple) distance measures for quantum operations is a subtle problem [25]. For simplicity, we quantify the proximity between a tomographically reconstructed process  $\mathcal{E}_{\text{meas}}$  and a target process  $\mathcal{E}_0$  by the mean fidelity:  $\mathcal{F}(\mathcal{E}_0[\rho_{\text{in}}], \mathcal{E}_{\text{meas}}[\rho_{\text{in}}])$ , where  $\mathcal{F}(\rho, \sigma) = \text{Tr}[\sqrt{\sqrt{\rho}\sigma\sqrt{\rho}}^2]$  is the Uhlmann fidelity between the density matrices  $\rho$  and  $\sigma$ ,  $\rho_{\text{in}} = |\Psi_{\text{in}}\rangle\langle\Psi_{\text{in}}|$ , and the overbar indicates average over an unbiased set of 36 input states [5]. Interestingly, this fidelity (contrary to the trace fidelity [19]) is unity if and only if  $\mathcal{E}_{\text{meas}} = \mathcal{E}_0$  regardless of whether the processes are unitary or not. For the identity process of Fig. 1, we find a mean fidelity of 0.95(2), where the error is the standard deviation on the set of the 36 eigenstates of  $\sigma_i \otimes \sigma_j$ , with  $i, j \in \{x, y, z\}$  used in the average. While a single Rabi flop on the micromotion sideband was performed with a success probability of 0.99(1), we observed that this efficiency slowly decreases with time if the axial displacement is not re-adjusted. This is likely due to slow drifts of stray fields (estimated to be  $\sim 10$  V/m/min). Furthermore, small laser detuning errors tend to reduce the single-qubit rotation fidelity.

Next we apply our tomography protocol to analyze a Mølmer-Sørensen interaction. The gate is performed on the  $|S\rangle \rightarrow |D\rangle$  transition via two sidebands, which are generated by applying two rf signals into an AOM switch [26], with frequencies of  $\omega_c \pm (\delta + \epsilon)$ , where  $\omega_c$  is the carrier transition

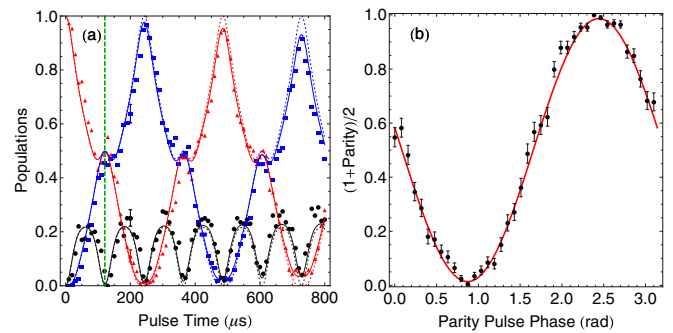


FIG. 2. (Color online) A Mølmer-Sørensen entangling gate on a ground-state cooled two-ion chain. (a) Evolution of the populations  $P_0$  (blue squares),  $P_1$  (black circles), and  $P_2$  (red triangles) as a function of the interaction duration. The dashed lines are the analytical solutions of the MS model [13]; the solid lines also take into account depolarization (see text). For clarity, single error bars are shown for  $t = 200$   $\mu$ s. (b) Parity scan (parity =  $P_0 + P_2 - P_1$ ) oscillation, obtained by scanning the phase of a  $\pi/2$  pulse after a gate time of  $t_g = 130$   $\mu$ s. The red solid line corresponds to the parameters extracted from a maximum-likelihood analysis of the data (see text). Each data point corresponds to 200 repetitions. All error bars of this panel are the binomial standard errors.

frequency,  $\delta$  is a motional sideband used for the intermediate spin-motion entanglement, and  $\epsilon$  is the gate detuning. We use the stretch axial mode at a frequency of  $\sqrt{3}\omega_z = 2\pi \times 1.679$  MHz for entanglement as it is less sensitive to heating than the center-of-mass mode [27]. The gate detuning is optimally set according to the Rabi frequency  $\Omega$ , as  $\eta\Omega = \epsilon/4$ , where  $\eta \approx 0.03$  is the motional Lamb-Dicke parameter, and the gate time is  $t_g = 2\pi/\epsilon$ . After resolved-sideband ground-state cooling of the stretch mode, the two ions are initialized by optical pumping to  $|SS\rangle$  (with single-ion error  $\sim 10^{-3}$  [28]). The gate generates the maximally entangled state  $|\Phi\rangle = (|SS\rangle + i|DD\rangle)/\sqrt{2}$ . In Fig. 2(a), we display the evolution of  $P_0$  (blue squares),  $P_1$  (black circles), and  $P_2$  (red triangles), obtained for a gate detuning of  $\epsilon = 2\pi \times 7.7$  kHz. At a pulse time of  $130\ \mu\text{s}$  (shown by a vertical dashed green line), the two ions are maximally entangled. There are several methods to extract the coherences of a two-ion density matrix from a parity scan. While a least-square fit usually gives a more optimistic result, it suffers from drawbacks, such as a possibility for unphysical results [29]. We rather adopted a more conservative maximum-likelihood analysis, and under the assumption of perfectly distinguishable parity measurements, we use a binomial distribution function [29]. We determine a parity contrast of  $C_p = 0.972(6)$  [red line of Fig. 2(b)]. Together with  $P_1(t_g) = 0.01(1)$ , we deduce a Bell-state production fidelity of  $\mathcal{F}(|\Phi\rangle\langle\Phi|, \rho_{\text{exp}}) = \frac{1}{2}(1 - P_1 + C_p) = 0.981(6)$ .

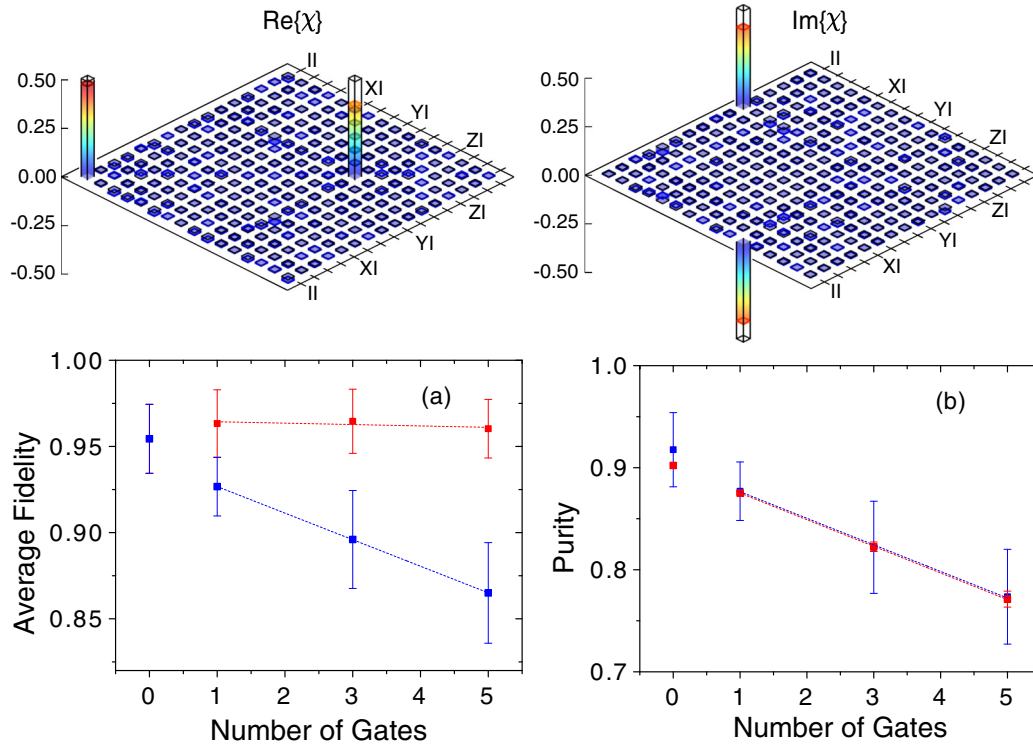


FIG. 3. (Color online) Process tomography of a Mølmer-Sørensen interaction. Upper panel: Real and imaginary parts of the reconstructed process matrix  $\text{Re}[\chi]$  and  $\text{Im}[\chi]$  of five consecutive gates. Lower panel: (a) Average fidelity. In blue points, the values extracted from the experimentally reconstructed  $\chi$  matrices with respect to the target gate operation  $\mathcal{E}_0$ . In red points, the mean values are calculated with respect to output density matrices for which a depolarizing operation has been applied. Dashed lines are linear fits. (b) Average state purity. In blue points, calculated from the reconstructed process  $\chi$  matrices, and in red from a depolarization channel model with a depolarization rate of  $1.9(1) \times 10^{-2}$  per gate time. The offset value being due to tomographic error, it is set arbitrarily on the red points, and is not used for the analysis of the gate. Error bars represent the standard deviation with respect to all input states (see text).

After calibrating the gate time, we experimentally reconstructed the  $\chi$ -process matrices of a single, three, and five consecutive MS gates (the latter is shown in the upper panel of Fig. 3). As 15 measurements are done to quantum-state analyze each of the 16 input states, and assuming 400 repetitions per experiment, a full process tomography totals  $240 \times 400 = 96\,000$  measurements. The target process matrices can be readily deduced from the analytically known evolution operator  $U(t)$  of two ions interacting with the bichromatic field [26]. At integer multiples  $n$  of the gate time  $t_g$ , the spin part of the evolution operator takes the simple form  $U_{\text{MS}}(n) \equiv U(nt_g) = \exp[-i(n\pi/8)(\sigma_y^{(1)} + \sigma_y^{(2)})^2]$ , whereas the motional part of the evolution operator equals the identity. The  $\chi$  matrix is calculated by expanding the exponent of  $U_{\text{MS}}$ , i.e.,  $U_{\text{MS}}(1) = 1/\sqrt{2}(I \otimes I + iY \otimes Y)$ . Plugging this expression into Eq. (1), we readily find

$$\begin{aligned} (\chi^{\text{MS}})_{II,II} &= (\chi^{\text{MS}})_{YY,YY} = 1/2, \\ (\chi^{\text{MS}})_{II,YY} &= -(\chi^{\text{MS}})_{YY,II} = i/2. \end{aligned} \quad (2)$$

Interestingly, this operation matrix, with four nonzero elements, is the simplest one describing entanglement in a separable-state basis (see, for comparison, the 16 nontrivial elements of the process-analyzed CNOT or *i*SWAP gates in the  $\sigma$ -operator basis [3,6]). The process matrix shown in Fig. 3 exhibits the four nonzero elements as expected from Eq. (2).

We now turn to a quantitative analysis of  $\chi^{\text{MS}}$ . The mean fidelity of  $\mathcal{E}_{\text{meas}}$  with respect to the map  $\mathcal{E}_0(nt_g)[\rho_{\text{in}}] = U_{\text{MS}}(n)\rho_{\text{in}}U_{\text{MS}}^\dagger(n)$  versus the number of applied gates  $n$  is shown by blue points in Fig. 3(a). Due to gate imperfections the fidelity decreases with growing number of applied gates at a rate of  $\approx 1.5 \times 10^{-2}$  per gate. The direct interpretation of imperfections from the process matrix is notoriously difficult because in the  $\sigma$  operator basis each noise process involves multiple elements with various weights. Instead, it is common to compare the measured process to different noise models [3,6,30]. Since the noise is assumed to be a small perturbation of the ideal evolution, we describe our nonideal process by the map  $\mathcal{E}(t)[\rho] = [1 - p(t)]\mathcal{E}_0(t)[\rho] + p(t)\mathcal{E}_{\text{noise}}[\rho]$ , where  $p(t)$  is the probability of error. Guided by the previous observation of fast ( $\sim 1$  MHz) laser phase noise on our master laser, driving incoherent  $S \rightarrow D$  transitions [22], we model the noisy process by a collective depolarization channel  $\mathcal{E}_{\text{noise}}[\rho] = \mathcal{E}_{\text{CD}}[\rho]$ , where  $\mathcal{E}_{\text{CD}}[\rho_{\text{in}}] = \int dU U^{\otimes 2} \rho_{\text{in}} U^\dagger \otimes 2$ , and  $dU$  is the Haar measure on  $U(2)$  [31–33]. This channel acts as a projector on the ( $U^{\otimes 2}$ -isotropic) Werner states:  $\mathcal{E}_{\text{CD}}[\rho_{\text{in}}] = W_{\alpha(\rho_{\text{in}})}$  where the Werner state is  $W_\beta = (1 - \beta)I/4 + \beta|\Psi_-\rangle\langle\Psi_-|$ ,  $\alpha(\rho_{\text{in}}) = \frac{1}{3}(4\langle\Psi_-|\rho_{\text{in}}|\Psi_-\rangle - 1)$ , and  $|\Psi_-\rangle = (|z\bar{z}\rangle - |\bar{z}z\rangle)/\sqrt{2}$  is the singlet Bell state. For a weak noise, it is reasonable to assume a linear expansion for the error,  $p(t) = \alpha_{\text{CD}}t$ , and the single free parameter of the model,  $\alpha_{\text{CD}}$ , can be determined from the purity of our measured processes, which is affected only by nonunitary operations. We recall that the purity of state  $\sigma$  is  $\mathcal{P}(\sigma) = \text{Tr}[\sigma^2]$ . The rate of depolarization is determined by matching the slope (with respect to the number of gates) of  $\overline{\mathcal{P}(\mathcal{E}(t)[\rho_{\text{in}}])}$  [red points in Fig. 3(b)] with the experimental purities  $\overline{\mathcal{P}(\mathcal{E}_{\text{meas}}[\rho_{\text{in}}])}$  [blue points in Fig. 3(b)]. The slope matches our data for a rate of  $\alpha_{\text{CD}} = 1.9(1) \times 10^{-2}$  per gate time. The identity process is excluded from these fits; since errors from tomography and the gates have a different origin, they are largely independent.

We can assess the relevance of this description by calculating the fidelity of  $\mathcal{E}_{\text{meas}}$  with respect to an MS interaction that has suffered partial depolarization  $\overline{\mathcal{F}(\mathcal{E}(nt_g)[\rho_{\text{in}}], \mathcal{E}_{\text{meas}}[\rho_{\text{in}}])}$  [red points of Fig. 3(a)]. Remarkably, we find that for the rate previously determined from the averaged purity, the mean fidelity to the partially depolarized states is almost constant as a function of the number of gates applied (residual rate is  $< 10^{-3}$  per gate). This shows that the depolarizing channel accounts well for the imperfections introduced by successive applications of gates, and we estimate that the remaining error is due to the tomography itself. Moreover, we can use this model to predict the expected imperfections on the population time dynamics previously measured in Fig. 2. On one hand, these contain more limited information than the full process matrices, namely, only the diagonal elements of the output state starting from  $\rho_{\text{in}} = |SS\rangle\langle SS|$ , but on the other hand, they are free from tomographic errors. While the solution of the perfect MS propagator (dashed lines in Fig. 2) does not describe our data well for the longest times, the agreement is excellent when the depolarization is taken into account (solid lines), without any adjustable parameter. Within this model we expect at  $t = t_g$  a Bell-state production fidelity of 98.7% starting from  $|SS\rangle$ , in good agreement with the direct measurement of 0.981(6). The measured depolarization rate is in rough agreement with the off-resonance  $S \leftrightarrow D$  incoherent transfer rate we observe on a single trapped ion. A more thorough study of the cause for depolarization is under way.

This research was supported by the Israeli Science Foundation, the Minerva Foundation, the German-Israeli Foundation for Scientific Research, the Crown Photonics Center, the Wolfson Family Charitable Trust, Yeda-Sela Center for Basic Research, David Dickstein of France, and M. Kushner Schnur of Mexico.

---

[1] A. Barenco, C. H. Bennett, R. Cleve, D. P. DiVincenzo, N. Margolus, P. Shor, T. Sleator, J. A. Smolin, and H. Weinfurter, *Phys. Rev. A* **52**, 3457 (1995).

[2] N. Kiesel, C. Schmid, U. Weber, R. Ursin, and H. Weinfurter, *Phys. Rev. Lett.* **95**, 210505 (2005).

[3] A. M. Childs, I. L. Chuang, and D. W. Leung, *Phys. Rev. A* **64**, 012314 (2001).

[4] M. Riebe, K. Kim, P. Schindler, T. Monz, P. O. Schmidt, T. K. Körber, W. Hänsel, H. Häffner, C. F. Roos, and R. Blatt, *Phys. Rev. Lett.* **97**, 220407 (2006).

[5] J. Home, D. Hanneke, J. Jost, J. Amini, D. Leibfried, and D. Wineland, *Science* **325**, 1227 (2009).

[6] R. Bialczak, M. Ansmann, M. Hofheinz, E. Lucero, M. Neeley, A. O’Connell, D. Sank, H. Wang, J. Wenner, and M. Steffen, *Nat. Phys.* **6**, 409 (2010).

[7] A. Sørensen and K. Mølmer, *Phys. Rev. Lett.* **82**, 1971 (1999).

[8] C. Sackett, D. Kielpinski, B. King, C. Langer, V. Meyer, C. Myatt, M. Rowe, Q. Turchette, W. Itano, and D. Wineland, *Nature (London)* **404**, 256 (2000).

[9] D. Leibfried, B. DeMarco, V. Meyer, D. Lucas, M. Barrett, J. Britton, W. Itano, B. Jelenkovic, C. Langer, and T. Rosenband, *Nature (London)* **422**, 412 (2003).

[10] B. P. Lanyon *et al.*, *Science* **334**, 57 (2011).

[11] K. Kim, M.-S. Chang, R. Islam, S. Korenblit, L.-M. Duan, and C. Monroe, *Phys. Rev. Lett.* **103**, 120502 (2009).

[12] J. Benhelm, G. Kirchmair, C. Roos, and R. Blatt, *Nat. Phys.* **4**, 463 (2008).

[13] G. Kirchmair, J. Benhelm, F. Zähringer, R. Gerritsma, C. Roos, and R. Blatt, *New J. Phys.* **11**, 023002 (2009).

[14] T. Monz, P. Schindler, J. T. Barreiro, M. Chwalla, D. Nigg, W. A. Coish, M. Harlander, W. Hänsel, M. Hennrich, and R. Blatt, *Phys. Rev. Lett.* **106**, 130506 (2011).

[15] Q. A. Turchette, C. S. Wood, B. E. King, C. J. Myatt, D. Leibfried, W. M. Itano, C. Monroe, and D. J. Wineland, *Phys. Rev. Lett.* **81**, 3631 (1998).

[16] U. Warring, C. Ospelkaus, Y. Colombe, R. Jördens, D. Leibfried, and D. J. Wineland, *Phys. Rev. Lett.* **110**, 173002 (2013).

[17] N. Navon, S. Kotler, N. Akerman, Y. Glickman, I. Almog, and R. Ozeri, *Phys. Rev. Lett.* **111**, 073001 (2013).

[18] J. F. Poyatos, J. I. Cirac, and P. Zoller, *Phys. Rev. Lett.* **78**, 390 (1997).

[19] M. Nielsen and I. Chuang, *Quantum Computation and Quantum Information* (Cambridge University Press, Cambridge, UK, 2010).

[20] N. Akerman, Y. Glickman, S. Kotler, A. Keselman, and R. Ozeri, *Appl. Phys. B* **107**, 1167 (2012).

[21] V. Letchumanan, M. A. Wilson, P. Gill, and A. G. Sinclair, *Phys. Rev. A* **72**, 012509 (2005).

[22] Y. Glickman, Ph.D. thesis, Weizmann Institute of Science, 2012.

[23] D. Leibfried, *Phys. Rev. A* **60**, R3335(R) (1999).

[24] Z. Hradil, *Phys. Rev. A* **55**, R1561 (1997).

[25] A. Gilchrist, N. K. Langford, and M. A. Nielsen, *Phys. Rev. A* **71**, 062310 (2005).

[26] C. Roos, *New J. Phys.* **10**, 013002 (2008).

[27] B. E. King, C. S. Wood, C. J. Myatt, Q. A. Turchette, D. Leibfried, W. M. Itano, C. Monroe, and D. J. Wineland, *Phys. Rev. Lett.* **81**, 1525 (1998).

[28] A. Keselman, Y. Glickman, N. Akerman, S. Kotler, and R. Ozeri, *New J. Phys.* **13**, 073027 (2011).

[29] T. Monz, Ph.D. thesis, University of Innsbruck, 2011.

[30] A. G. Kofman and A. N. Korotkov, *Phys. Rev. A* **80**, 042103 (2009).

[31] R. F. Werner, *Phys. Rev. A* **40**, 4277 (1989).

[32] Another potentially relevant noise stems from limited  $T_2$ , which is described by a phase damping noise  $\mathcal{E}_{\text{noise}}[\rho] = \sum_{i \in \mathcal{S}} \hat{P}_i \rho \hat{P}_i$ , where  $\mathcal{S} = \{|SS\rangle, |SD\rangle, |DS\rangle, |DD\rangle\}$  and  $\hat{P}_i = |i\rangle \langle i|$ . This map does not describe our data well as in that case, the loss of fidelity results from a decay of coherences, not from a population mismatch.

[33] The map  $\mathcal{E}_{\text{CD}}$  bears strong similarities with the fully mixing depolarization map  $\mathcal{E}_{\text{FD}}[\rho] = \int dU dU' (U \otimes U') \rho (U^\dagger \otimes U'^\dagger) = (I \otimes I)/4$ . Indeed, for all separable input states that are orthogonal on the Bloch sphere,  $\mathcal{E}_{\text{CD}}$  is fully mixing. More quantitatively,  $\overline{\mathcal{F}(\mathcal{E}_{\text{FD}}[\rho], \mathcal{E}_{\text{CD}}[\rho])} = 0.97$ , and we found that for  $10^4$  Haar-drawn pure two-qubit states, 80% have a fidelity  $\mathcal{F}$  with the fully mixed state higher than 0.95, and 55% have  $\mathcal{F} > 0.98$ . As a result, the fully depolarizing channel also provides a good description of our data.